



Supporting Online Material for
**Covering a Broad Dynamic Range: Information Processing at the
Erythropoietin Receptor**

Verena Becker, Marcel Schilling, Julie Bachmann, Ute Baumann, Andreas Raue,
Thomas Maiwald, Jens Timmer, Ursula Klingmüller*

*To whom correspondence should be addressed. E-mail: u.klingmueller@dkfz-heidelberg.de

Published 20 May 2010 on *Science* Express
DOI: 10.1126/science.1184913

This PDF file includes:

Materials and Methods
SOM Text
Figs. S1 to S16
References

Materials and Methods

Plasmids and reagents. Retroviral expression vectors were pMOWS-puro (*S1*). To yield hemagglutinin (HA)-tagged murine EpoR (pMOWS-HA-mEpoR), an *EcoRI/BamHI* fragment from the vector pMX-EpoR-HA-IRES-GFP (provided by S. Constantinescu, Ludwig Institute for Cancer Research, Brussels, Belgium) was inserted into the *PacI/BamHI* restriction sites of pMOWS-mEpoR (*S2*) and a Kozak consensus sequence was introduced 5' of the EpoR cDNA. To generate pMOWS-SBP-mEpoR, the HA-tag from pMOWS-HA-mEpoR was exchanged with a streptavidin binding peptide (SBP)-tag (*S3*). Human EpoR was extracted from a human fetal liver plasmid cDNA library (Stratagene) and inserted into pMOWS-puro with a Kozak consensus sequence. To yield pMOWS-HA-hEpoR, the HA-tag was inserted by using the forward primer 5'-taccatacgcacgtccagactacgccccggaccccaagttcg-3' and the reverse primer 5'-ggcgtagctcgggacgtcgtagggtagaggttagcgggggc-3'. All clones were verified by sequence analysis. In general, prior to experiments cell surface expression of HA-EpoR in stably transduced BaF3 cells was tested by flow cytometry analysis.

Cells were either treated with Epo (Epoetin alfa, Janssen-Cilag), NESP (Novel Erythropoiesis Stimulating Protein, Amgen), or murine interleukin (IL)3 (R&D Systems).

Cells lines and primary cells. The Phoenix eco packaging cell line (*S4*) was cultured in DMEM (Invitrogen) including 10% FCS (Invitrogen). BaF3 cells (*S5*) were cultured in RPMI 1640 (Invitrogen) including 10% FCS and supplemented with 10% WEHI-conditioned medium as a source of IL3. All media were supplemented with penicillin (100 U/ml) and streptomycin (100 mg/ml). CFU-E cells of d13.5 embryos from wild-type Balb/c mice were enriched as described (*S1*), additionally using antibodies to YBM/42 (*S6*) and to Gr1 (Pharmingen) in the sorting procedure.

Transfections of Phoenix eco cells were performed by calcium phosphate precipitation. Transducing supernatants were generated 24 hours after transfection by passing through a 0.45 µm filter and supplemented with 8 µg/ml polybrene (Sigma). Stably transduced BaF3 cells expressing HA-tagged murine EpoR (BaF3-EpoR cells), SBP-tagged murine EpoR (BaF3-SBP-EpoR cells), or HA-tagged human EpoR (BaF3-hEpoR cells) were selected in the presence of 1.5 µg/ml puromycin (Sigma) 48 hours after transduction.

Binding assays. 1×10^6 BaF3-EpoR cells were incubated with 10 pM, 100 pM, 250 pM, 500 pM, or 2000 pM [125 I]-Epo ([125 I]-Epoetin alfa, GE Healthcare) in 100 µl RPMI 1640 (Invitrogen) supplemented with 10% FCS (Invitrogen) for 4 hours at 21°C. To separate free [125 I]-Epo, cells were centrifuged through a layer of FCS and cell-bound as well as free

[¹²⁵I]-Epo was measured in a Cobra gamma counter (Packard). Specific binding was determined by subtracting the mean value (n=3) of cells incubated with both [¹²⁵I]-Epo and 250 U/ml unlabeled Epo from the radioactivity of cells incubated without unlabeled Epo. Results are presented with fitting a one-site saturation regression (Michaelis-Menten function) and as a Scatchard plot.

To determine the affinity of streptavidin (SAv) to SBP-EpoR, 1×10^6 BaF3-SBP-EpoR cells were washed with biotin-free RPMI 1640 (PAN Biotech) and resuspended in 100 μ l SAv binding medium (biotin-free RPMI 1640 supplemented with 1 mM L-Glutamine (Invitrogen) and 25 mM HEPES pH 7.4). Cells were incubated with 100 pM, 250 pM, 1000 pM, 2500 pM, or 5000 pM [¹²⁵I]-SAv (GE Healthcare) for 4 hours at 21°C. Cells were washed with biotin-free RPMI 1640 and pooled supernatants as well as cells were measured in a Cobra gamma counter. To determine specific binding, control cells were additionally incubated with 2.5 μ M unlabeled SAv (Sigma). Results are presented with fitting a one-site saturation regression (Michaelis-Menten function).

Endocytosis assays. 4×10^6 BaF3-EpoR cells were washed, starved in RPMI 1640 (Invitrogen) supplemented with 1 mg/ml BSA (Sigma) for 3 hours, and stimulated with 2100 pM [¹²⁵I]-Epo (approximately equal to 5 U/ml) ([¹²⁵I]-Epoetin alfa, GE Healthcare) in 100 μ l RPMI 1640 for the indicated time at 37°C. After stimulation, cells were immediately transferred to ice and free [¹²⁵I]-Epo was separated from the cells by centrifugation through a layer of FCS (Invitrogen). Cell surface bound [¹²⁵I]-Epo was stripped by incubation with 4% acetic acid for 5 min on ice and subsequent centrifugation through FCS. The efficiency of acid stripping was approximately 95% and membrane integrity after acid stripping was confirmed by Trypan blue exclusion. Samples were measured in a Cobra gamma counter (Packard). Specific binding was determined by subtracting the mean value (n=3) of cells incubated with both [¹²⁵I]-Epo and 500 U/ml unlabeled Epo.

To access constitutive receptor endocytosis, 1×10^6 BaF3-SBP-EpoR cells were washed with biotin-free RPMI 1640 (PAN Biotech) and starved in SAv binding medium (biotin-free RPMI 1640 supplemented with 1 mM L-Glutamine (Invitrogen) and 25 mM HEPES pH 7.4) supplemented with 1 mg/ml BSA (Sigma) for 1 hour. Cells were subsequently incubated with 1000 pM [¹²⁵I]-SAv (GE Healthcare) in 100 μ l SAv binding medium for the indicated time at 37°C. After stimulation, cells were immediately transferred to ice and washed three times with 500 μ l biotin-free RPMI 1640 to separate unbound [¹²⁵I]-SAv from the cells. Cell surface bound [¹²⁵I]-SAv was stripped by incubation with 4% acetic acid for 5 min on ice and subsequent washing steps. Samples were measured in a Cobra gamma counter. Specific binding was determined by subtracting the mean value (n=3) of cells additionally incubated with 2.5 μ M unlabeled SAv (Sigma).

Proliferation assay. To show the capacity of signaling and biological responses mediated by HA-EpoR and SBP-EpoR, BaF3-EpoR cells, BaF3-SBP-EpoR cells or BaF3 cells mock-transduced with the empty vector were washed three times with RPMI 1640 (Invitrogen) and seeded at densities of 3.85×10^4 cells/well in 24-well plates in the presence of Epo concentrations ranging from 0.1 to 5 U/ml or in medium without Epo. After 4 days, cell numbers were determined using a Coulter counter (Beckman Coulter). Results are

expressed as cell number/ml. To ensure that cells were seeded with comparable densities, cells were cultivated in medium supplemented with WEHI as a source for IL3 in parallel wells and after 4 days cell numbers for the different stable cell lines were within the same range.

Starvation, treatment, and stimulation of cells. 1×10^7 BaF3-EpoR cells (fig. S8B, upper panel, and figs. S8D and S16B) or BaF3-hEpoR cells (fig. S8B, lower panel) were washed and starved in RPMI 1640 (Invitrogen) supplemented with 1 mg/ml BSA (Sigma) for 3 hours and subsequently stimulated with 5 U/ml Epo (approximately equivalent to 2100 pM) or 2100 pM NESP for the times indicated at 37°C or left unstimulated. For dose-response time course analysis, cells were stimulated with 1, 2.5, 5, 10 or 25 U/ml Epo for the times indicated at 37°C or left unstimulated (Fig. 4B and figs. S10 and S11). To study the restimulating capacity, cells were stimulated with 5 U/ml Epo at 37°C and if indicated cells were restimulated with 50 U/ml Epo (Fig. 3A).

To stimulate cells with depleted medium, 1×10^7 BaF3-EpoR cells or BaF3 cells mock-transduced with the empty vector as control were washed and starved in RPMI 1640 supplemented with 1 mg/ml BSA for 3 hours. Cells were subsequently stimulated for up to 5 hours at 37°C and the culture medium was collected at the indicated time points. Subsequently, 1×10^7 freshly starved BaF3-EpoR cells were centrifuged, resuspended in the collected culture medium, and stimulated for 10 min each at 37°C. In addition, 1×10^7 BaF3-EpoR cells were stimulated with fresh ligand or left unstimulated (Fig. 3B and figs. S8A and S16C).

To examine the effect of inhibited transport of EpoR from intracellular pools to the plasma membrane, 1×10^7 BaF3-EpoR cells were washed and starved in RPMI 1640 supplemented with 1 mg/ml BSA for 3 hours. Cells were treated with 10 µg/ml Brefeldin A (Sigma; stock 5 mg/ml in ethanol) for 30 min at 37°C and subsequently stimulated with 5 U/ml Epo for up to 5 hours at 37°C. As control, cells were treated with 0.2% ethanol before stimulation. Cell viability was confirmed by Trypan blue exclusion (fig. S13, B and C).

To exclude SAV-mediated EpoR activation, 1×10^7 BaF3-SBP-EpoR cells or BaF3 cells mock-transduced with the empty vector were washed with biotin-free RPMI 1640 (PAN Biotech) and starved in SAV binding medium (biotin-free RPMI 1640 supplemented with 1 mM L-Glutamine (Invitrogen) and 25 mM HEPES pH 7.4) supplemented with 1 mg/ml BSA (Sigma) for 3 hours. Cells were stimulated with the indicated concentrations of Epo or SAV (Sigma) for 10 min at 37°C or left unstimulated (fig. S3B).

To examine IL3-mediated signaling, 1×10^7 parental BaF3 cells were washed and starved in RPMI 1640 (Invitrogen) supplemented with 1 mg/ml BSA (Sigma) for 3 hours. For analysis of IL3 depletion, cells were subsequently stimulated with recombinant 50 ng/ml murine IL3 for the times indicated at 37°C or left unstimulated (fig. S9A). To study the restimulating capacity, 1×10^7 BaF3 cells were stimulated with 10 ng/ml IL3 and if indicated cells were restimulated with 100 ng/ml IL3 (fig. S9B).

After enrichment of CFU-E cells from the fetal liver, CFU-E cells were cultivated in IMDM (Invitrogen) supplemented with 30% FCS (Invitrogen) and 0.5 U/ml Epo for 14 hours. 1×10^7 CFU-E cells were washed and starved in Panserin 401 (PAN Biotech)

supplemented with 1 mg/ml BSA for 1 hour, and cells were subsequently stimulated with 1 U/ml Epo at 37°C (fig. S8C).

Immunoprecipitation and quantitative immunoblotting. For analysis of ligand in medium, the culture medium of stimulated cells was collected at the indicated time points and Epo, NESP, or IL3 were immunoprecipitated with antibodies to Epo (R&D Systems, clone 9C21D11) or IL3 (R&D Systems, clone MP28F8). Immunoprecipitates were eluted by boiling in 2× sample buffer (4% SDS, 100 mM Tris pH 7.4, 20% glycerol, 10% β -mercaptoethanol, 200 mM DTT, 0.02% bromophenolblue) for 3 min at 95°C, separated by 15% SDS-PAGE (Epo, NESP) or 17.5% SDS-PAGE (IL3) and transferred to a PVDF membrane (Millipore). Proteins were immobilized with Ponceau S solution (Sigma) and membranes were incubated with mouse antibodies to Epo (R&D Systems, clone AE7A5) or goat antibodies to IL3 (R&D Systems) as primary antibodies and subsequently with horseradish peroxidase-coupled anti-mouse (GE Healthcare) or anti-goat antibodies (Santa Cruz) as secondary antibodies. For experiments yielding ten or more consecutive samples (figs. S8D and S9A), randomized non-chronological gel loading was performed to minimize the correlated error of protein transfer to the membrane (S7).

For analysis of phosphorylated EpoR, JAK2, or IL3 receptor, cells were lysed with 2× NP-40 lysis buffer (2% NP-40, 300 mM NaCl, 40 mM Tris pH 7.4, 20 mM NaF, 2 mM EDTA pH 8.0, 2 mM ZnCl₂ pH 4.0, 2 mM MgCl₂, 2 mM Na₃VO₄, 20% glycerol) supplemented with aprotinin and AEBSF (Sigma). Immunoprecipitations were performed with antibodies to EpoR (Santa Cruz, M-20), JAK2 (Upstate), or IL3 receptor (Santa Cruz, K-19), adding a standard of purified GSTΔEpoR (40 ng) or GST-JH1JH2 (20 ng) harboring the respective antibody binding epitope if appropriate (S7). Immunoprecipitates were eluted by boiling in 2× sample buffer for 3 min at 95°C, separated by 10% SDS-PAGE and transferred to a nitrocellulose membrane (Schleicher & Schuell). To examine differently glycosylated forms of the EpoR, immunoprecipitates were treated with glycoprotein denaturing buffer (New England Biolabs) for 10 min at 95°C, digested with the endoglycosidase EndoH (New England Biolabs) for 1 hour at 37°C or left untreated, boiled in 4× sample buffer for 3 min at 95°C, separated by 10% SDS-PAGE and transferred to a nitrocellulose membrane (fig. S12B). For experiments analyzing ten or more consecutive samples (fig. S10), randomized non-chronological gel loading was performed to minimize the correlated error of protein transfer to the membrane (S7). Proteins were immobilized with Ponceau S solution and membranes were incubated with mouse antibodies to phosphotyrosine (pTyr) (Upstate, clone 4G10) and horseradish peroxidase-coupled anti-mouse antibodies (GE Healthcare). To remove antibodies, membranes were treated with β -mercaptoethanol and SDS (S8) and subsequently incubated with rabbit antibodies to EpoR or IL3 receptor and horseradish peroxidase-coupled protein A (GE Healthcare) or with mouse antibodies to JAK2 (MBL International, clone 691R5) and horseradish peroxidase-coupled anti-mouse antibodies (GE Healthcare).

Detection was performed using enhanced chemiluminescence (GE Healthcare). Immunoblot data were acquired with the CCD camera-based LumiImager (Roche Diagnostics) and quantification was performed with the LumiAnalyst software (Roche Diagnostics). Immunoblot data were processed using GelInspector (S7).

To calculate the amount of phosphorylated EpoR and JAK2 integrated over time, a smoothing spline approximation was applied to quantitative immunoblot data and integration was performed until the spline curve-estimated amount of phosphorylated proteins dropped below a threshold set to 10% of maximal activation measured for stimulation with 25 U/ml Epo.

Mathematical modeling. For developing and calibration of mathematical models, the modeling software PottersWheel (S9) was used. Parameter estimation was performed in logarithmized parameter space using a trust region optimization method. For each fit, up to 200 iterations were run with a χ^2 tolerance of 10^{-7} and fit parameter tolerance of 10^{-7} . For all parameter estimation procedures, χ^2 values of the best fit showed good agreement with the experimental data.

For the ‘core model’ and the ‘auxiliary model’, the parameter values for K_D and K_{D_SAV} as well as B_{max} and B_{max_SAV} were fixed to the experimentally determined values. Ligand association rates k_{on} and k_{on_SAV} were estimated within boundaries $10^{-7} \text{ pM}^{-1} \times \text{min}^{-1}$ and $10^3 \text{ pM}^{-1} \times \text{min}^{-1}$, all other parameters within boundaries between 10^{-7} min^{-1} and 10^3 min^{-1} , and none of the finally estimated parameters lay on these boundaries (fig. S4B). The initial values for EpoR were set to the experimentally determined B_{max} or B_{max_SAV} , while the initial values for *Epo* and *SAV* were estimated within boundaries of $\pm 10\%$ of the concentrations used in the experimental setup. Parameter estimation was performed simultaneously for both the ‘core model’ and the ‘auxiliary model’ that share three parameters and 1σ confidence intervals were calculated for parameters of the best fit by exploiting the profile likelihood (fig. S4B, column ‘Best fits and confidence intervals’) (S10). Estimated parameters for an independent data set for the ‘core model’ were comparable to parameter values displayed in fig. S4B. The mathematical models presented here will be made available to the public on the BioModels Database (www.ebi.ac.uk/biomodels). To calculate the amount of cell surface Epo-EpoR complexes integrated over time, integration was performed until the amount of Epo-EpoR complexes reached a threshold of 5.16 pM (1% of unoccupied EpoR at time $t=0$) and maximal integration time was set to 1080 min. This time threshold is rationalized by the doubling time of BaF3 cells of approximately 16 to 18 hours.

For estimating ligand-binding rates based on immunoblot data, all parameters of the ‘core model’ were fixed to the estimated values (fig. S4B) except k_{on} and k_{off} that were estimated within boundaries between $10^{-7} \text{ pM}^{-1} \times \text{min}^{-1}$ and $10^3 \text{ pM}^{-1} \times \text{min}^{-1}$ or 10^{-7} min^{-1} and 10^3 min^{-1} , respectively. For estimation of ligand-binding rates of Epo, three data sets for direct measurement of ligand from the culture medium of stimulated BaF3-EpoR cells were scaled and the mean is displayed with a linear error model (comprising a relative and an absolute error based on the standard deviation of the data) (S7). For estimation of ligand-binding rates for NESP, two data sets each for direct measurement of ligand from the culture medium of stimulated BaF3-EpoR cells or for phosphorylated EpoR of cells stimulated with depleted medium were displayed as mean of two replicates with a linear error model. Immunoblot data were included in the ‘core model’ as the dynamic variable ‘Epo’ (fig. S2A, ‘core model’) using a scaling parameter. For NESP, multi-experiment

parameter estimation was performed. In order to determine simultaneous 1σ confidence intervals for k_{on} and k_{off} , contour plots of iso-log-likelihood levels (*S11*, *S12*) were used.

Identifiability analysis. To test for structurally non-identifiable parameters that cannot be determined unambiguously, an identifiability analysis based on a non-parametric bootstrap-based algorithm was applied (*S13*). To this aim, 5000 fits with start values for parameters randomly generated from the entire parameter space were performed. Using the best 5% based on χ^2 values in order to avoid the problem of local optima, these fits were analyzed non-parametrically for relations between parameters that would indicate structural non-identifiability, and none were found for both the ‘core model’ and the ‘auxiliary model’. In addition, analysis of the best 5% of these 5000 fits was used to calculate the mean and the variance of these parameter estimates, confirming that parameter estimation yielded a global optimum (fig. S4B, column ‘Identifiability’). Further analysis was performed using the profile likelihood (*S10*) to confirm structural and practical identifiability and to derive confidence intervals for the parameter estimates (fig. S4B, column ‘Best fits and confidence intervals’).

Model-based determination of half-life. In order to determine the half-life of EpoR, Epo-EpoR, and Epo-EpoR_i, we created three versions of the original mathematical ‘core model’ to simulate the behavior of a hypothetical label, which is added onto each of the species of interest. In order to avoid double counting, species were only allowed to enter the initially labeled pool by loosing their labeling. The half-life $T_{1/2}(t)$ was determined as $T_{1/2}(t) = t' - t$, with t' being the time point where the amount of labeled species dropped below half of its value at time point t . The approach has been applied using the PottersWheel modeling framework (*S9*).

Sensitivity analysis. Sensitivity analysis was applied to investigate relative changes of derived system quantities K as a result of relative infinitesimal changes in parameter values p_i . Control coefficients were calculated by:

$$S_{p_i}^K = \frac{p_i}{K} \cdot \frac{\partial K}{\partial p_i}$$

Hornberg et al. (*S14*) derived summation laws for control coefficients of derived system quantities like signal amplitude, signal duration, and area under curve. The proofs for the summation laws (*S15*) can be extended to show the existence of summation laws for the system target quantities investigated in our approach.

$$\begin{aligned} \sum_i S_{p_i}^{\text{amplitude}} &= 0 \\ \sum_i S_{p_i}^{\text{peak time}} &= -1 \\ \sum_i S_{p_i}^{\text{signal duration}} &= -1 \end{aligned}$$

$$\sum_i S_{p_i}^{\text{integral signal}} = -1$$

Parameter values were estimated with 1σ confidence intervals (fig. S4B). To exclude that uncertainties in parameter estimates influenced the results, sensitivity analysis was not only performed for parameter values of the best fit, but additionally for upper and lower boundaries of confidence intervals for the three parameters displaying the largest confidence intervals (k_t , k_{ex} , and k_{dl}). This analysis included all possible combinations of one, two, or three of these parameters giving rise to a $3 \times 3 \times 3$ matrix. The results of this analysis revealed that control coefficients were only marginally changed compared to results yielded from parameter values for the best fit.

SOM Text

Background information on potential mechanisms contributing to EpoR endocytosis

Ligand-induced EpoR endocytosis is dependent on the WSXWS motif within the extracellular domain (*S16*) as well as on membrane-proximal cytoplasmic residues (*S17*, *18*). Endocytosis of ligand-receptor complexes has been proposed to terminate signaling by removing receptors from the cell surface including partial receptor degradation in the proteasome and routing of the remaining receptor along with Epo to lysosomes (*S19*). Endocytosis and degradation of Epo-EpoR complexes establish a route for Epo clearance from the body (*S20*).

Recently, it has been shown that in response to ligand binding cell surface EpoR is endocytosed in a clathrin-mediated manner and both JAK2 kinase activity and EpoR cytoplasmic tyrosines are important for ligand-induced EpoR endocytosis in the JAK2-deficient fibrosarcoma cell line γ 2a (*S21*). However, this subject is controversially discussed as there are also studies showing that ligand-induced EpoR endocytosis is dependent on a membrane-proximal intracellular motif (*S17*) and another study reports that EpoR endocytosis in hematopoietic 32D cells is independent of JAK2 kinase activity and receptor activation (*S22*). Therefore, mechanisms of receptor endocytosis may strongly depend on the cellular context.

The ubiquitin ligase β -Trcp was identified to mediate EpoR ubiquitination (*S23*). However, Meyer and colleagues demonstrated that endocytosis and lysosomal routing do not depend on receptor ubiquitination. Therefore, these studies suggest that EpoR association with ubiquitin ligases modulates the cellular response upon Epo stimulation, but does not influence receptor and ligand trafficking.

To our knowledge, the only study regarding ligand-independent EpoR endocytosis was performed by Beckman and colleagues (*S22*), suggesting that endocytosis occurs with a similar rate as pinocytosis of cell surface glycoproteins.

Ligand-induced receptor mobilization and recycling as well as receptor turnover are highly dynamic and tightly intertwined processes. Due to the interdependency of the secretory and endocytic pathway, these processes are difficult to disentangle experimentally. Compounds used to manipulate receptor trafficking often simultaneously affect multiple targets. For example, phenyl arsine oxide (PAO) not only blocks endocytosis of cell surface receptors, but also inhibits tyrosine phosphatases. Therefore, we combined time-resolved quantitative data with mathematical modeling to determine reaction fluxes of receptor and ligand species.

Hypothetical strategies facilitating linear information processing

A linear dose-to-signal conversion by cell surface receptors can in principle be achieved by several hypothetical strategies (Fig. 1, B to D) that might contribute to a different extent:

(i) 'mobilization': Ligand-induced mobilization by transport of newly synthesized EpoR from intracellular receptor pools to the plasma membrane as a putative mechanism of information processing was motivated by observations for chemokine receptor 3 that in response to IgE activation is mobilized to the plasma membrane from intracellular storage pools in granula (*S24*). The EpoR has been observed to reside in large intracellular pools

(S25). We integrated EpoR mobilization to the plasma membrane in response to ligand binding as a single parameter k_{mob} into our mathematical model to summarize its overall effect, including chaperone action mediated by JAK2 (S26).

(ii) 'recycling': Recycling of receptor endocytosed in response to ligand binding to repopulate the plasma membrane was considered since experimental evidence for such processes has been reported for tumor necrosis factor receptor (S27).

(iii) 'turnover': Constant receptor turnover comprising both ligand-independent transport of newly synthesized receptor from intracellular pools to the plasma membrane and ligand-independent receptor endocytosis has been shown for the leptin receptor (S28). Similarly, the EpoR is endocytosed in a ligand-independent manner (S22) and displays large intracellular receptor pools (S25).

Principally, constitutively high levels of cell surface expression of receptors as observed for the epidermal growth factor receptor (EGFR) with up to 100000 molecules per cell (S29) could contribute to the detection of extensive ligand concentrations. However, we exclude high cell surface abundance as a major strategy employed by the EpoR. Epo transcription is controlled by the oxygen partial pressure and at basal conditions, plasma levels of Epo are within the range of 15 mU/ml (S30) and at these low levels, primary erythroid progenitor cells with approximately 1000 Epo binding sites (S31) display a relatively high EpoR abundance. Yet, acute concentrations of plasma levels are observed to rise up to 10000 mU/ml Epo and therefore, high receptor abundance at the plasma membrane is lost under these conditions. In our experimental BaF3-EpoR cell line, abundance of EpoR at the plasma membrane is rather low with approximately 7800 binding sites (fig. S1) compared to the EGFR.

Establishing an SBP-tagged EpoR for ligand-independent endocytosis

To measure ligand-independent EpoR endocytosis, we replaced the HA tag of murine HA-EpoR (S32) with an SBP tag (S3), which comprises 38 amino acids and therefore is considerably smaller than e.g. a GST tag (220 amino acids), but rather comparable in size to the HA tag comprising 9 amino acids.

To confirm functionality of the SBP-tagged EpoR, stably transduced BaF3 cells were stimulated with different concentrations of Epo or SAV (fig. S3B). This experiment demonstrated that the SBP-tagged EpoR was not activated upon SAV stimulation, but receptor phosphorylation was already strongly induced by stimulation with 5 U/ml Epo, a concentration that was used for biochemical analysis of signaling in this study. To compare the capacity of SBP-tagged EpoR with HA-tagged EpoR to support Epo-mediated proliferation, BaF3-EpoR cells or BaF3-SBP-EpoR cells were seeded in medium supplemented with Epo and cell numbers were determined after 4 days of cultivation (fig. S3C). The results of this Epo dose-response profile revealed that both receptor variants supported proliferation to the same extent, confirming that the SBP-tagged EpoR appears to function similarly to HA-EpoR.

Applying [^{125}I]-SAV to BaF3-SBP-EpoR cells revealed parameter values for both $K_{\text{D,SAV}}$ and $B_{\text{max,SAV}}$ (fig. S3A) as well as the kinetics of ligand-independent EpoR endocytosis (fig. S3D, right panel). The low concentration of endocytosed SAV reflects the poor affinity ($K_{\text{D,SAV}}$) of SAV to SBP-EpoR (fig. S3A) rather than a decreased endocytosis efficiency of

SBP-tagged EpoR. The measured value for the dissociation constant K_{D_SAV} of 2964 pM is similar to the K_D value of 2500 pM observed in the initial study describing the use of an SBP tag (S3). Additionally, the ratio of ligand-induced and ligand-independent EpoR endocytosis estimated by our modeling approach (fig. S4B) is comparable to the ratio reported in a study in which surface glycoproteins were labeled with [3H]-galactose and the EpoR was immunoprecipitated to determine the amount of endocytosed receptor after 40 min (S22).

Model-based determination of half-life of EpoR subpopulations

The biochemically determined half-life of 45 min for glycosylated EpoR (S33) reflects the effects of multiple processes such as transport, plasma membrane residence, and degradation. Using our mathematical ‘core model’, we calculated the individual time-dependent half-life of EpoR-containing species in a specific subcompartment. Due to the non-linearity of the system (fig. S2A), the half-life of EpoR and Epo-EpoR complexes at the cell surface changed over time, whereas it was constant for endocytosed Epo-EpoR due to the linearity of the involved reactions (fig. S7). At the beginning of stimulation, a half-life of 3 to 4 min was predicted for EpoR, but due to decreasing Epo concentrations the half-life of EpoR increased until reaching a plateau of 21 min reflecting receptor turnover (k_i). Cell surface Epo-EpoR complexes were predicted to have a half-life of 9 to 10 min in early-phase stimulation, providing a time frame for sampling and integrating extracellular Epo. The half-life results in peak amounts of cell surface Epo-EpoR within the range of 9 to 10 min (Fig. 2B and Fig. 2C, right panel), coinciding with the maximum EpoR phosphorylation (fig. S11) and therefore suggesting that ligand-induced endocytosis (k_e) has an important role in shaping early-response kinetics of EpoR activation.

Rapid Epo depletion in the culture medium

Model simulations predicted that intact Epo is rapidly depleted from the medium by endocytosis-mediated uptake and subsequent degradation and ligand is consumed after 5 hours of stimulation (Fig. 2C, left panel). Moreover, the model predicted that the majority of endocytosed Epo is degraded and subsequently released into the extracellular medium (dEpo_e), whereas only a minor fraction is retained intracellularly (dEpo_i). Degraded products that are secreted may include both peptide fragments and free [^{125}I]. The massive release of these degraded products into the medium correlates with the measurement of total extracellular [^{125}I]-Epo (Fig. 2B, left panel), which represents both intact ligand and degradation products.

Epo depletion in the culture medium can in principle be monitored by trichloroacetic acid (TCA) precipitation of [^{125}I]-Epo. However, cleavage products of Epo might be produced before final lysosomal degradation as observed for IL3 (S34) and these fragments might precipitate as well. Therefore, this method is not suitable to distinguish larger fragments from intact, biologically active Epo. Rather, separation according to the molecular weight is required as achieved by immunoblot analysis. In our immunoblot experiments, we combined chemiluminescence with CCD camera-based detection and quantification since we could show that this allows for linear detection over a broad dynamic range (S7). This method in combination with directly immunoprecipitating ligand from the medium enabled

us to demonstrate that extracellular Epo is degraded in the context of BaF3 cells expressing murine or human EpoR (fig. S8B). A detailed quantitative analysis of Epo depletion was performed in triplicates (fig. S8D, upper panels) with an increased sampling rate. Experimental data were displayed with error bars applying a linear error model and could be described by an exponential decay function (fig. S8D, lower panel), reinforcing rapid Epo depletion in the medium. Primary erythroid progenitor cells at the CFU-E stage stimulated with 1 U/ml Epo depleted ligand as well (fig. S8C), although with slower dynamics compared to BaF3-EpoR cells, which could be explained by an approximately 10-fold lower EpoR cell surface expression in primary cells compared to BaF3-EpoR cells. Fast Epo depletion from the extracellular environment can be explained by the slow dissociation of Epo from its receptor ($k_{\text{off}}=0.0172 \text{ min}^{-1}$) in conjunction with a considerably higher rate for ligand-induced EpoR endocytosis ($k_e=0.075 \text{ min}^{-1}$). In combination with the rate of receptor turnover, the remaining amount of intact Epo in the medium influences the kinetics of EpoR recovery at the plasma membrane. Extracellular Epo stimulates enhanced endocytosis of EpoR engaged in ligand-receptor complexes compared to ligand-independent receptor endocytosis of unoccupied EpoR. For example, after 2 hours of stimulation with 5 U/ml Epo, 24% of initial ligand was still present in the extracellular medium (Fig. 2C, left panel), whereas unoccupied EpoR at the plasma membrane recovered to 51% of its initial value (Fig. 2C, right panel). Thus, re-setting the system in terms of maximal expression of unoccupied EpoR on the cell surface requires complete ligand depletion.

Comparison of EpoR and EGFR systems properties

As a prime example for receptor tyrosine kinases (RTK) and relevance in many diseases, the epidermal growth factor receptor (EGFR) has been studied in much detail. It has been shown that upon EGF stimulation, the EGFR is rapidly endocytosed and subsequently depleted from the cell surface by lysosomal degradation (S35). The rate of ligand-independent endocytosis of the EGFR ($k_i=0.02 \text{ min}^{-1}$) (S36) is lower compared to the EpoR ($k_i=0.033 \text{ min}^{-1}$) as determined by our studies. Furthermore, since the rate of ligand-induced receptor endocytosis is two-fold higher for the EGFR ($k_e=0.15 \text{ min}^{-1}$) compared to the EpoR ($k_e=0.075 \text{ min}^{-1}$), the ratio of ligand-induced receptor endocytosis to ligand-independent receptor endocytosis, defined as endocytic downregulation D (S37), is considerably higher for the EGF-EGFR system ($D=7.5$) (S37) than for the EpoR ($D=2.3$). Therefore, in contrast to the EGFR for which ligand-induced loss of cell surface receptors attenuates signaling (S38), the low rate of EpoR endocytic downregulation indicates a less prominent contribution of ligand-induced receptor removal from the plasma membrane to regulate long-term EpoR activity. Thus, whereas for the EGFR high levels of cell surface expression of EGFR (S29) in combination with a high a rate of endocytic downregulation (S37) have been observed, the EpoR shows both a low cell surface abundance (S31) (fig. S1) and a low rate of endocytic downregulation, illustrating that these receptors employ different strategies.

Despite these distinct properties, the time frame to initiate signaling at the plasma membrane is within the range of 5 to 10 min for both receptor systems as determined for the EGFR by co-localization studies (S39) and for the EpoR by model-based calculation of

the half-life of EpoR subpopulations in our study. However, Epo-EpoR dissociation is considerably slower than that of EGF-EGFR complexes (*S40*). As a consequence, the ratio of ligand-induced endocytosis k_e and ligand dissociation k_{off} is increased for the EpoR compared to that of the EGFR (*S36*), thus facilitating efficient ligand depletion from the cell surface and, thereby, high temporal resolution (*S41*) of Epo concentrations. Analysis of the mathematical model demonstrates the extent to which the parameters k_e and k_{off} contribute to the Epo-EpoR flux (fig. S6).

Ligand and receptor dynamics in IL3 signaling

To address whether characteristic properties uncovered for the EpoR system such as rapid ligand depletion and receptor recovery can be observed for other cytokine receptors, we quantitatively monitored the IL3 receptor endogenously expressed in our model cell line BaF3. Distinct from the homodimeric EpoR, the IL3 receptor is a hetero-oligomeric receptor composed of a cytokine-specific α chain as well as a common beta chain (β_c) that is not only part of the IL3 receptor but shared with receptor complexes binding IL-5 and GM-CSF. To measure the kinetics of ligand depletion, IL3 was immunoprecipitated from the culture medium of BaF3 cells stimulated with IL3 and analyzed by quantitative immunoblotting (fig. S9A). Similar to Epo (fig. S8D), IL3 was depleted from the extracellular medium, showing a rapid decline within the first 10 min of stimulation (fig. S9A, lower panel). To test whether the IL3 receptor is capable of being restimulated, we measured the activation dynamics of the receptor in a time course experiment (fig. S9B). Phosphorylation of the IL3 receptor beta chain as well as JAK2 peaked at approximately 5 min and rapidly returned to basal levels at 20 and 60 min. Restimulation was achieved for both the receptor and JAK2 with additional ligand stimulation 10 min before cell lysis. Previously, cellular desensitization to IL3 stimulation has been controversially discussed since it has been reported that desensitization occurs after pre-incubation with other common beta chain-engaging cytokines (IL-5, GM-CSF) (*S42*), whereas other studies did not observe such an effect (*S34*). Our results show that adding an excess of ligand to the BaF3 cells resulted in a rapid loss of receptor protein as well as reduction in JAK2 (Fig. S9B), suggesting that a large fraction of IL3 receptor beta chain is accessibly to ligand and therefore present at the cell surface. Remarkably, expression of total IL3 receptor beta chain in BaF3 cells strongly increased between 20 and 180 min after stimulation, thereby potentially compensating for the ligand-induced loss of receptor and preventing a refractory state. Therefore, similar to the EpoR, rapid ligand depletion and receptor recovery are key properties of the IL3 receptor system. However, our results indicate that instead of being facilitated by large intracellular pools as for the EpoR this may be achieved by IL3-induced synthesis of receptor. Thus, the EpoR and IL3 receptor employ different strategies to accomplish a similar overall systems behavior.

Assigning an essential role to large intracellular pools of the EpoR

The EpoR resides in large intracellular pools and only a minor fraction reaches the cell surface in both primary cells with endogenous EpoR expression and cell lines exogenously expressing EpoR (*S25*, *S33*, *S43-S45*). The presence of the EpoR in intracellular compartments has been demonstrated by immunofluorescence studies for multiple cell lines

including NIH3T3 and BaF3 cells expressing the EpoR (S33) as well as for NIH3T3 and CFU-E cells expressing a GFP-tagged EpoR (S46, S47). Our mathematical model provides evidence that these large intracellular receptor pools serve as a reservoir for continuous replenishment of EpoR on the plasma membrane. To support this, we quantitatively assessed the impact of ligand on the amount of the EpoR, a major fraction of which is localized in intracellular compartments. We quantified the amount of total receptor present in BaF3-EpoR cells stimulated with different ligand concentrations for up to 5 hours (fig. S10). This analysis showed that neither at very high ligand concentrations nor during prolonged exposure to ligand a depletion of total EpoR was observed (fig. S12A). Further, to specifically examine a potential effect of Epo on intracellular receptor pools, BaF3-EpoR cells were stimulated with Epo and samples were either left untreated or were subjected to digestion with the endoglycosidase EndoH. In a subsequent analysis by quantitative immunoblotting, the amount of the EndoH-sensitive EpoR form was determined that reflects the unglycosylated and immature glycosylated EpoR and therefore represents receptors localized in intracellular pools (fig. S12B, upper panel, unglycosylated EpoR of EndoH-digested samples). This quantification demonstrated that the amount of intracellular EpoR in the endoplasmic reticulum and early Golgi compartments represented a major fraction of the total EpoR present in the cells and stayed constant over time, independent of ligand stimulation (fig. S12B, lower panel). Especially, no decrease in intracellular EpoR pools could be observed, arguing against depletion due to ligand-induced mobilization of EpoR to the plasma membrane. Therefore, these experiments underpin the role of intracellular receptor pools as a large EpoR reservoir and corroborate model-based evidence excluding ligand-induced mobilization by transport of newly synthesized EpoR from intracellular receptor pools to the plasma membrane as a major strategy contributing to EpoR signaling (fig. S5). On the contrary, our results for the IL3 receptor system indicated that a large fraction of the IL3 receptor beta chain was present on the plasma membrane and rapid loss of receptor upon IL3 stimulation was compensated by ligand-induced receptor synthesis (fig. S9B). Thus, both cytokine receptors, the EpoR and the IL3 receptor, employ different strategies to support receptor expression on the plasma membrane, with the EpoR relying on large intracellular receptor pools that are not affected by ligand stimulation.

To assess the contribution of intracellular receptor pools to signal integration, we examined the impact of reducing the transport rate of receptors from intracellular pools to the plasma membrane. Due to the non-linear dynamics of the Epo-EpoR system, we used model simulations to predict the effect of reduced receptor transport on experimentally addressable populations and thereby guide experimental validation. By employing the ‘core model’ (fig. S13A, upper panel), we simulated the dynamic behavior of Epo-EpoR complexes at the plasma membrane and of Epo in the culture medium for different transport rate values (k_{tr}). The model predicted a reduction in both the peak amplitude and the integrated amount of cell surface Epo-EpoR complexes for lower rates of receptor transport (fig. S13A, lower left panel). Additionally, a decreased transport of receptor to the plasma membrane was also predicted to result in a substantially slower depletion of Epo from the culture medium (fig. S13A, lower right panel).

To experimentally validate the model predictions and inhibit transport of EpoR from intracellular pools to the plasma membrane, BaF3-EpoR cells were treated with Brefeldin A before stimulation with Epo. In agreement with model simulations for cell surface Epo-EpoR complexes indicative for the receptor population that can be converted into phosphorylated EpoR (Fig. 4, A and B), time course analysis revealed that the receptor was phosphorylated in Brefeldin A-treated cells, but that the integrated amount of activated EpoR was reduced compared to mock-treated cells ('ctrl') (fig. S13B). A 32 percent reduction of the peak amplitude of activated EpoR in Brefeldin A-treated cells was observed. This reduction is due to inhibition of EpoR transport to the plasma membrane during both Epo stimulation and pretreatment with Brefeldin A. The latter effect caused a gradual loss of cell surface EpoR by ongoing ligand-independent endocytosis that is not captured in the model simulations. Additionally, an increase of total EpoR was observed as consequence of Brefeldin A treatment of the cells (fig. S13B, left panel) since EpoR transport to the plasma membrane is reduced and thus, the receptor accumulates in intracellular compartments. In line with our model predictions showing that inhibition of receptor transport has a major effect on ligand depletion, the analysis of immunoprecipitated ligand from the medium revealed that in contrast to mock-treated control cells, receptor-mediated Epo degradation in Brefeldin A-treated cells was dramatically decreased and ligand was still present at high levels after 300 min of stimulation (fig. S13C). Comparison of data (fig. S13C, right panel) and model simulations (fig. S13A, lower right panel) indicated an efficiency to inhibit receptor transport to the plasma membrane of approximately 90%. The initial decrease of Epo in the model predictions, which was not observed in the experimental data, is due to the fact that simulations did not take into account that pretreatment with the inhibitor reduced the amount of cell surface EpoR. As shown in restimulation experiments, in the absence of the inhibitor blocking receptor transport BaF3-EpoR cells remained ligand-responsive (Fig. 3A) due to a replenishment of cell surface EpoR (Fig. 2C). Despite high ligand concentrations in the culture medium of Brefeldin A-treated cells (fig. S13C), receptor phosphorylation was only detectable for early but not for later time points (fig. S13B). Thus, these experiments confirm an essential role of large intracellular EpoR pools and substantiate our model-based evidence that transport of receptor from intracellular pools of the endoplasmic reticulum and the Golgi apparatus is a prerequisite to sample and integrate extracellular ligand, thereby enabling linear signal integration for a broad range of ligand concentrations.

Sensitivity analysis

Since ligand concentration critically determines the onset of signaling, we performed a sensitivity analysis with respect to the amount of biologically active Epo integrated over time. Calculating control coefficients (S14, S15) showed that both the turnover rate k_t and the ligand association rate k_{on} exerted a major influence on the amount of intact Epo (fig. S14A), whereas the other parameters showed only minor control. Together with the parameter k_{ex} describing ligand and receptor recycling, k_t and k_{on} were also important for the kinetics of unoccupied EpoR at the plasma membrane (fig. S14B) and cell surface Epo-EpoR complexes (fig. S14C). Moreover, the rate for ligand-induced endocytosis k_e was

especially important for the peak time and the amount of cell surface Epo-EpoR complexes integrated over time.

Bioavailability and bioactivity of erythropoiesis-stimulating agents

There is intense research on developing advanced erythropoiesis-stimulating agents (ESA) for clinical applications that display altered ligand-binding kinetics to increase the serum half-life and thereby reduce dosing intervals in patients (S48). Sensitivity analysis for the integral of intact extracellular ligand showed that not k_{off} and therefore not the dissociation constant K_D , but rather k_{on} displayed the largest control on various target quantities of Epo and EpoR dynamics (fig. S14). However, with decreasing values for the ligand association parameter k_{on} , the influence of the dissociation rate k_{off} was increasing. Therefore, we simulated the integral of intact Epo as well as cell surface Epo-EpoR complexes for various $k_{\text{on}}/k_{\text{off}}$ couples and assigned the terms bioavailability and bioactivity to these target quantities, respectively. The definition of bioactivity is rationalized by the linear relation of ligand concentration to both integral EpoR occupancy and EpoR as well as JAK2 activation (Fig. 4, A and B). Confirming the sensitivity analysis, simulations for these target quantities revealed that especially for low ligand association rate values k_{on} had a higher influence than k_{off} (fig. S15). The color gradients indicate a region of ligand-binding kinetics that displayed a trade-off between bioavailability and bioactivity, which is desirable for the development of ESA in pharmacological research. To exemplify these distinct properties, we combined mathematical modeling with immunoblot data for ligand depletion of Epo or the hyperglycosylated Epo derivative Novel Erythropoiesis Stimulating Protein (NESP) (S49). Based on the observation that only ligand-binding kinetics, but not the rate of endocytosis or intracellular ligand processing vary for Epo and NESP (S20), we used our model to estimate k_{on} and k_{off} for both ligand species (fig. S16). The results indicated that Epo possessed a high bioactivity but rather low bioavailability, whereas NESP was well situated within the suggested region showing a trade-off between bioavailability and bioactivity (fig. S15). Estimating k_{on} and k_{off} values and analyzing these parameters in respect to dynamic Epo and EpoR properties as shown here may provide a rationale in the choice of Epo derivatives for further in-depth analysis. Thus, this approach exemplifies how computational modeling might fuel a more rationalized and efficient development of therapeutic agents.

Supporting Figures

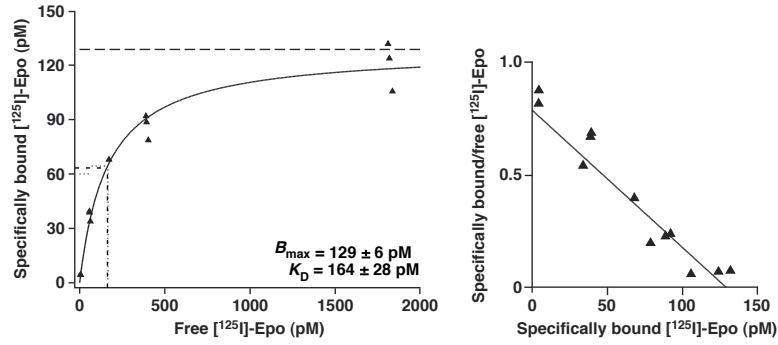


Fig. S1. Measurement of Epo binding sites on the plasma membrane. BaF3-EpoR cells were incubated with increasing concentrations of [125 I]-Epo. Specifically bound [125 I]-Epo was plotted versus free [125 I]-Epo. A one-site saturation regression (Michaelis-Menten function, solid line) was fitted to the data to determine B_{\max} (maximal binding, long dashed line) and K_D (free [125 I]-Epo concentration for half-maximal binding, short dashed line). B_{\max} was used to calculate the number of Epo binding sites (approximately 7800) on the plasma membrane of BaF3-EpoR cells (left panel). Scatchard analysis shows a linear relation (right panel).

A 'Core model' / 'Core model + k_{mob} '

Ordinary differential equations ('core model')	
EpoR	$\dot{x}_1 = k_1 \cdot B_{max} - k_1 \cdot x_1 - k_{on} \cdot x_1 \cdot x_2 + k_{off} \cdot x_3 + k_{ex} \cdot x_4$
Epo	$\dot{x}_2 = -k_{on} \cdot x_1 \cdot x_2 + k_{off} \cdot x_3 + k_{ex} \cdot x_4$
Epo-EpoR	$\dot{x}_3 = k_{on} \cdot x_1 \cdot x_2 - k_{off} \cdot x_3 - k_{ex} \cdot x_4$
Epo-EpoR _i	$\dot{x}_4 = k_{ex} \cdot x_3 - k_{ex} \cdot x_4 - k_{di} \cdot x_4 - k_{de} \cdot x_4$
dEpo _i	$\dot{x}_5 = k_{di} \cdot x_4$
dEpo _e	$\dot{x}_6 = k_{de} \cdot x_4$

Parameters

k_1	ligand-independent EpoR endocytosis
k_{mob}	ligand-induced EpoR mobilization
k_{on}	association of Epo and EpoR
k_{off}	dissociation of Epo and EpoR
K_D	dissociation constant for Epo-EpoR
k_{ex}	ligand-induced EpoR endocytosis
k_{di}	recycling of Epo and EpoR
k_{de}	degradation of ligand-EpoR complexes, remaining intracellular
k_{de}	degradation of ligand-EpoR complexes, secreted extracellular

Ordinary differential equations ('core model + k_{mob} ')	
EpoR	$\dot{x}_1 = k_1 \cdot B_{max} + k_{mob} \cdot x_3 - k_1 \cdot x_1 - k_{on} \cdot x_1 \cdot x_2 + k_{off} \cdot x_3 + k_{ex} \cdot x_4$
Epo	$\dot{x}_2 = -k_{on} \cdot x_1 \cdot x_2 + k_{off} \cdot x_3 + k_{ex} \cdot x_4$
Epo-EpoR	$\dot{x}_3 = k_{on} \cdot x_1 \cdot x_2 - k_{off} \cdot x_3 - k_{ex} \cdot x_4$
Epo-EpoR _i	$\dot{x}_4 = k_{ex} \cdot x_3 - k_{ex} \cdot x_4 - k_{di} \cdot x_4 - k_{de} \cdot x_4$
dEpo _i	$\dot{x}_5 = k_{di} \cdot x_4$
dEpo _e	$\dot{x}_6 = k_{de} \cdot x_4$

Assignment rules

k_{off}	$k_{off} = k_{on} \cdot K_D$
Nonzero initial values	
EpoR	$x_1 = B_{max}$ (t=0)
Epo	x_2 (t=0)

Observables

Epo in medium	$y_1 = x_2 + x_6$ (Epo + dEpo _e)
Epo on surface	$y_2 = x_3$ (Epo-EpoR)
Epo in cells	$y_3 = x_4 + x_5$ (Epo-EpoR _i + dEpo _i)

B 'Auxiliary model'

Ordinary differential equations	
EpoR	$\dot{x}_7 = k_1 \cdot B_{max_SAV} - k_1 \cdot x_7 - k_{on_SAV} \cdot x_7 \cdot x_8 + k_{off_SAV} \cdot x_9$
SAV	$\dot{x}_8 = -k_{on_SAV} \cdot x_7 \cdot x_8 + k_{off_SAV} \cdot x_9 + k_{ex_SAV} \cdot x_{10}$
SAV-EpoR	$\dot{x}_9 = k_{on_SAV} \cdot x_7 \cdot x_8 - k_{off_SAV} \cdot x_9 - k_1 \cdot x_9$
SAV-EpoR _i	$\dot{x}_{10} = k_1 \cdot x_9 - k_{ex_SAV} \cdot x_{10} - k_{di} \cdot x_{10} - k_{de} \cdot x_{10}$
dSAV _i	$\dot{x}_{11} = k_{di} \cdot x_{10}$
dSAV _e	$\dot{x}_{12} = k_{de} \cdot x_{10}$

Parameters

k_1	ligand-independent EpoR endocytosis
k_{on_SAV}	association of SAV and EpoR
k_{off_SAV}	dissociation of SAV and EpoR
K_{D_SAV}	dissociation constant for SAV-EpoR
k_{ex_SAV}	recycling of SAV
k_{di}	degradation of ligand-EpoR complexes, remaining intracellular
k_{de}	degradation of ligand-EpoR complexes, secreted extracellular

Assignment rules

k_{off_SAV}	$k_{off_SAV} = k_{on_SAV} \cdot K_{D_SAV}$
Nonzero initial values	
EpoR	$x_7 = B_{max_SAV}$ (t=0)
SAV	x_8 (t=0)

Observables

SAV in medium	$y_4 = x_8 + x_{12}$ (SAV + dSAV _e)
SAV on surface	$y_5 = x_9$ (SAV-EpoR)
SAV in cells	$y_6 = x_{10} + x_{11}$ (SAV-EpoR _i + dSAV _i)

Fig. S2. Non-linear system of ordinary differential equations. Ordinary differential equations, assignment rules, parameters, nonzero initial values as well as observables are given for dynamic mathematical models (A) for the two nested models 'core model' and 'core model + k_{mob} ', and (B) for the 'auxiliary model'. The 'core model + k_{mob} ' includes an additional parameter k_{mob} describing ligand-induced mobilization of newly synthesized intracellular EpoR pools to the plasma membrane. Parameters K_D and K_{D_SAV} as well as B_{max} and B_{max_SAV} were fixed to experimentally determined values. The initial values for EpoR were set to B_{max} or B_{max_SAV} and the initial values for the dynamic variables x_2 (Epo) and x_8 (SAV) were estimated within boundaries of $\pm 10\%$ of the concentrations used in the experimental setup.

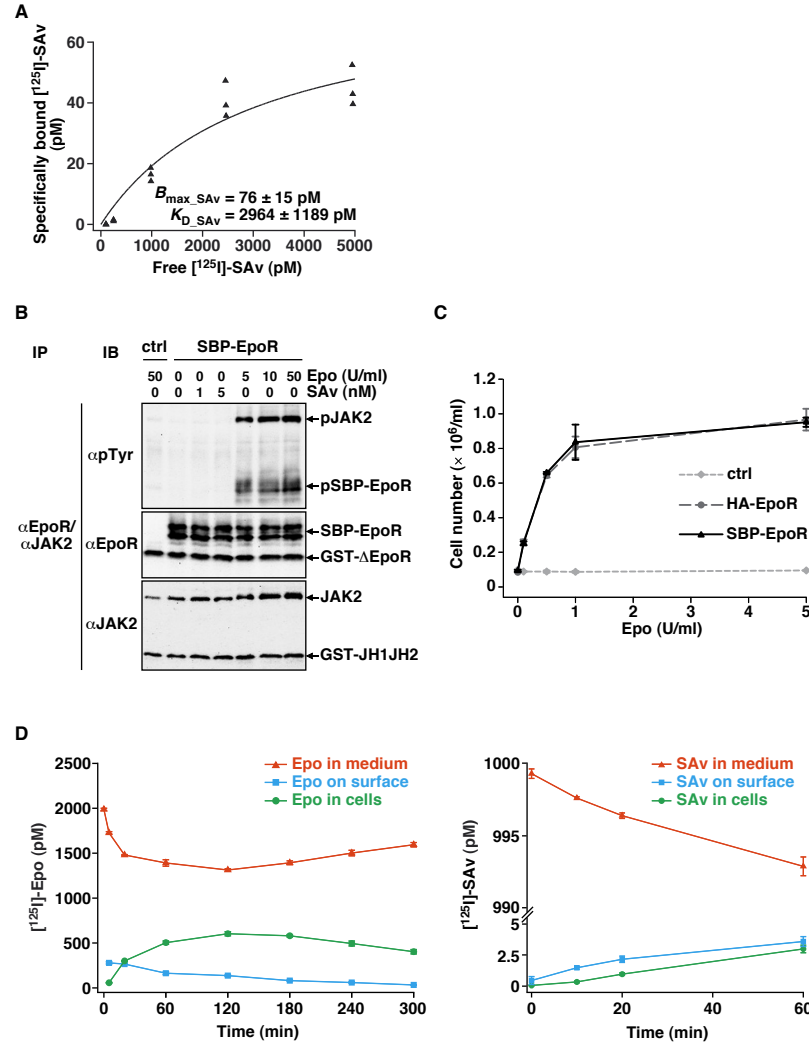


Fig. S3. Establishing SBP-EpoR. **(A)** BaF3-SBP-EpoR cells were incubated with increasing concentrations of [125 I]-SAv. Specifically bound [125 I]-SAv was plotted versus free [125 I]-SAv. A one-site saturation regression (Michaelis-Menten function) was fitted to the data to determine B_{\max_SAv} (maximal binding) and K_{D_SAv} (free [125 I]-SAv concentration for half-maximal binding). **(B)** Mock-transduced BaF3 cells (ctrl) or BaF3-SBP-EpoR cells were stimulated with Epo or SAV for 10 min or were left unstimulated. Immunoprecipitates (IP) were analyzed by quantitative immunoblotting (IB) with antibodies to phosphotyrosine (pTyr) and to EpoR or JAK2. **(C)** BaF3-EpoR or BaF3-SBP-EpoR cells were cultivated in medium supplemented with rising concentrations of Epo or without Epo. Mock-transduced cells were taken as control (ctrl). After 4 days, cell numbers were determined by Coulter Counter (mean \pm S.D., $n=3$). **(D)** BaF3-EpoR cells (left panel) or BaF3-SBP-EpoR cells (right panel) were incubated at 37°C with 2100 pM [125 I]-Epo or 1000 pM [125 I]-SAv, respectively. Unbound [125 I]-labeled ligand was measured (ligand in medium, red triangles),

cells were acid-stripped, and radioactivity in supernatants (ligand on surface, blue squares) as well as cell pellets (ligand in cells, green circles) was measured. Error bars represent standard deviations (n=3). pJAK2 and pSBP-EpoR, phosphorylated proteins; GST- Δ EpoR and GST-JH1JH2, recombinant GST-tagged proteins used as reference.

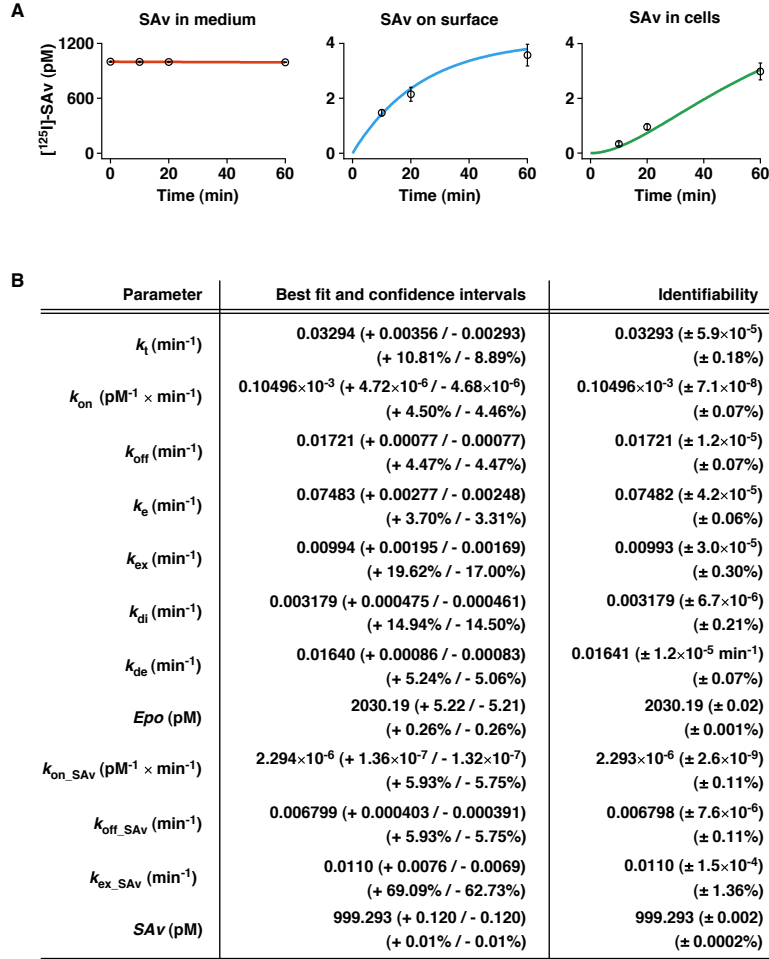


Fig. S4. Identifiability analysis and confidence intervals of estimated parameters. **(A)** Experimental data for the ‘auxiliary model’ are represented with standard deviations ($n=3$). Parameter estimation was performed simultaneously for both the ‘core model’ (Fig. 2B) and the ‘auxiliary model’ and trajectories of the best fit are shown. **(B)** Values of parameter estimates for both the ‘core model’ and the ‘auxiliary model’ including 1σ confidence intervals derived by the profile likelihood ($S10$) are displayed. In addition, mean value and variance of parameter estimates for the best 5% of 5000 fits based on χ^2 values indicate a global optimum.

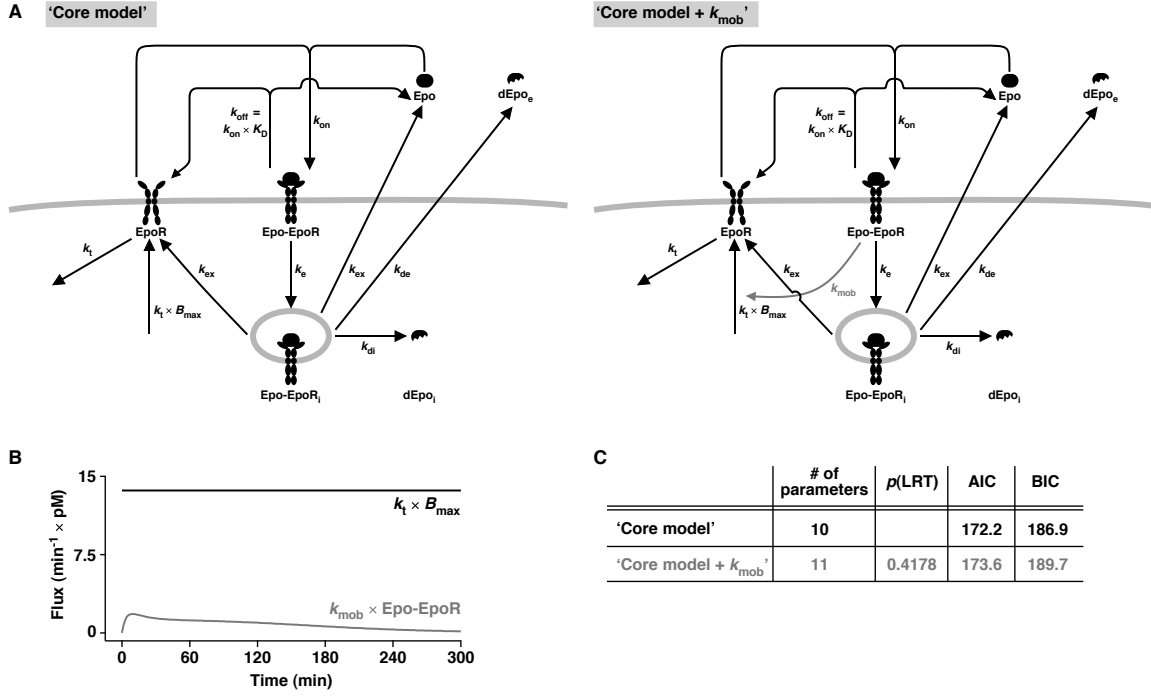


Fig. S5. Model discrimination for the 'core model' and the 'core model + k_{mob} '. **(A)** Graphical representation of the two nested models 'core model' (left panel) and 'core model + k_{mob} ' (right panel). **(B)** The flux of the reactions contributing to the replenishment of EpoR at the cell surface is depicted for the 'core model + k_{mob} '. **(C)** Statistical tests were performed to compare the performance and thereby discriminate the two nested models including a likelihood-ratio test (LRT) (S50) as well as the Akaike (AIC) (S51) and Bayesian Information Criterion (BIC) (S52). All three model selection criteria rank competing models by balancing model-data compliance and complexity of the model. Models with lower values for AIC and BIC are preferred, with the BIC showing a stronger penalty term for the number of estimated parameters than the AIC. The number of parameters is depicted as the sum of the parameters of the 'core model' and the 'auxiliary model' (10 parameters) or the 'core model + k_{mob} ' and the 'auxiliary model' (11 parameters) (fig. S2), which were calibrated simultaneously in a global multi-experiment fitting. An insignificant p value for the likelihood-ratio test (LRT) as well as the higher values for AIC and BIC for the 'core model + k_{mob} ' argue for the 'core model' in comparison to the 'core model + k_{mob} '.

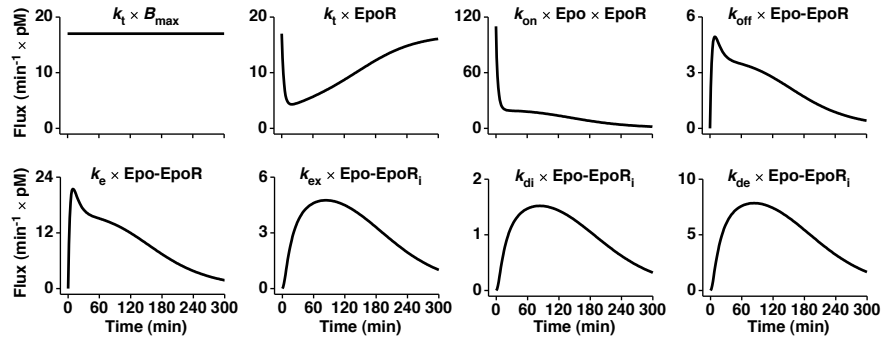


Fig. S6. Contribution of individual fluxes to ligand and receptor dynamics. Flux analysis revealed the individual contribution of the 8 primary reactions to the dynamics of Epo and EpoR subpopulations, which are depicted for the ‘core model’.

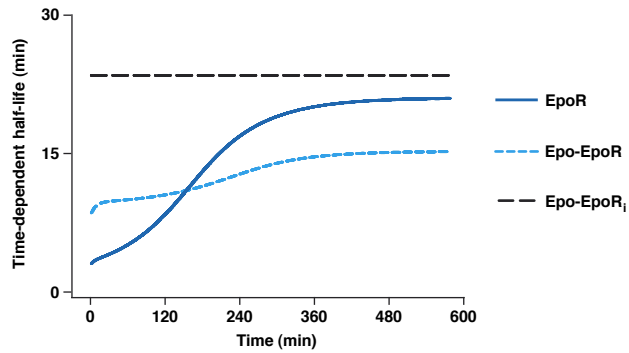


Fig. S7. Half-life of EpoR subpopulations. Using the underlying ‘core model’, the time-dependent half-life was calculated for EpoR and Epo-EpoR at the cell surface as well as for endocytosed Epo-EpoR complexes (Epo-EpoR_i).

progenitor cells were stimulated with Epo and the culture medium was collected at the indicated time points. **(D)** In a densely sampled time course, BaF3-EpoR cells were stimulated with Epo and the culture medium was collected at the indicated time points. The experiment was performed in triplicates and samples were loaded in a randomized order (*S7*) (upper panels). Immunoblot data were quantified using a CCD camera in combination with the LumiAnalyst software. Data processing was performed with GelInspector (*S7*) and data are displayed as mean (n=3) with a linear error model. An exponential decay function was fitted to the data. pEpoR, phosphorylated EpoR; GST-ΔEpoR, recombinant GST-tagged protein used as reference; mEpoR, murine EpoR; hEpoR, human EpoR; CFU-E, colony forming unit-erythroid.

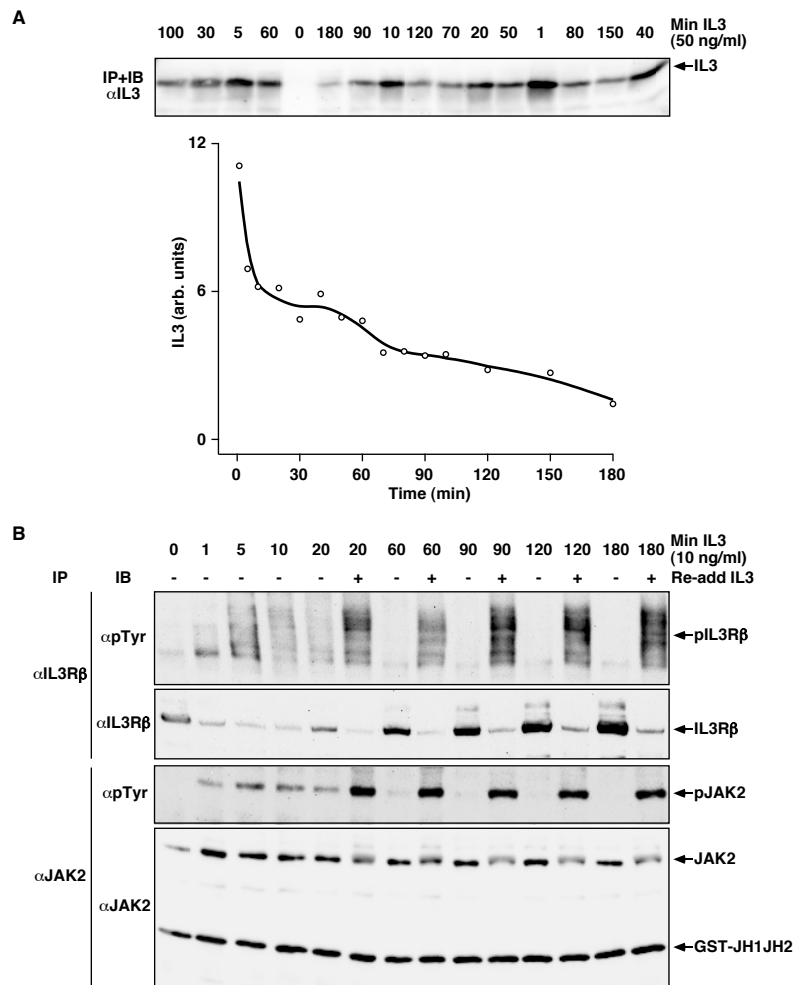


Fig. S9. Ligand and receptor dynamics in IL3 signaling. **(A)** Parental BaF3 cells were stimulated with IL3 and the culture medium was collected at the indicated time points. IL3 was immunoprecipitated (IP) from the medium and samples were loaded in randomized order (S7) and analyzed by quantitative immunoblotting (IB) with antibodies to IL3 (upper panel). Immunoprecipitated IL-3 was quantified and results (circles) are expressed as arbitrary units with a smoothing spline approximation (line) (lower panel). **(B)** Parental BaF3 cells were stimulated with 10 ng/ml IL3 and if indicated, 100 ng/ml IL3 was added to the cells 10 min before cell lysis. Immunoprecipitates (IP) were analyzed by quantitative immunoblotting (IB) with antibodies to phosphotyrosine (pTyr) and IL3 receptor. pIL3Rβ and pJAK2, phosphorylated proteins; GST-JH1JH2, recombinant GST-tagged protein used as reference.

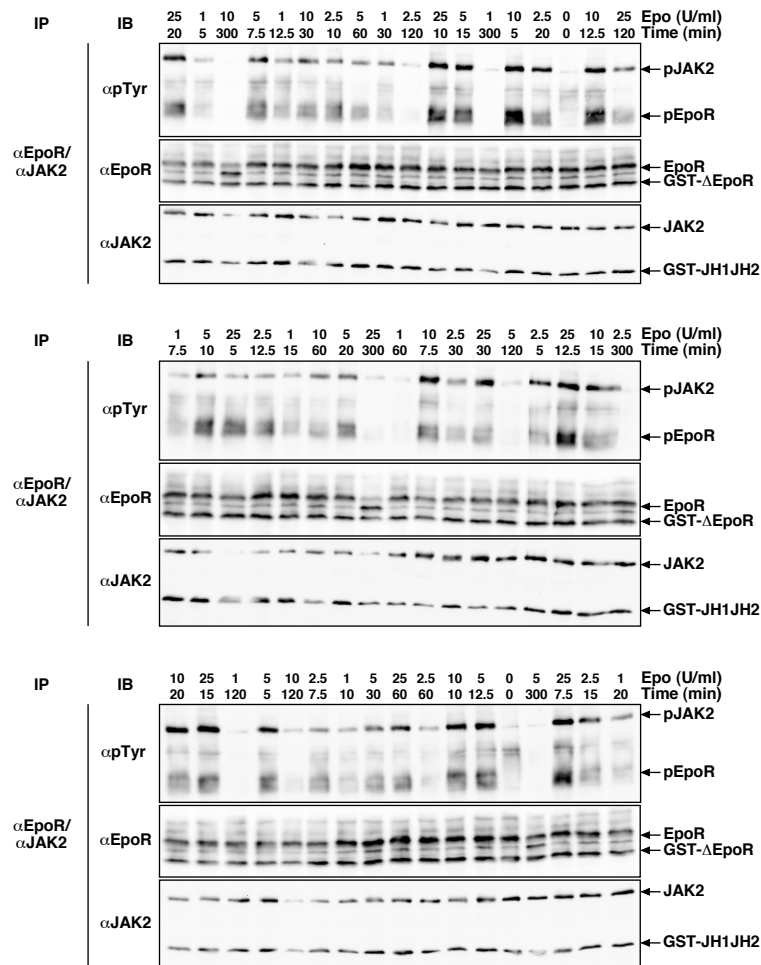


Fig. S10. Dose-response time course analysis of EpoR and JAK2 activation. BaF3-EpoR cells were stimulated with different Epo concentrations and lysed at the indicated time points. Immunoprecipitates (IP) were distributed on 3 gels in a randomized order (S7) and analyzed by quantitative immunoblotting (IB) with antibodies to phosphotyrosine (pTyr) as well as antibodies to JAK2 and EpoR. pJAK2 and pEpoR, phosphorylated proteins; GST-ΔEpoR and GST-JH1JH2, recombinant GST-tagged proteins used as reference.

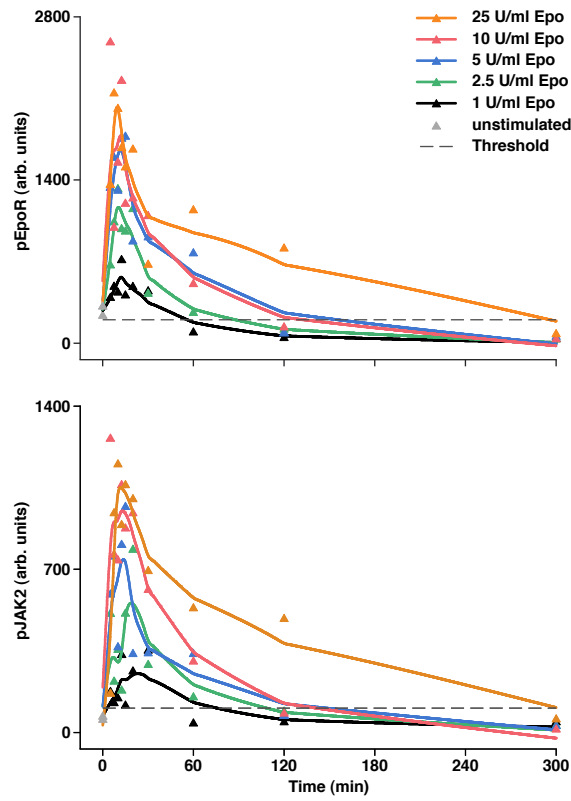


Fig. S11. Quantification of dose-response time course analysis of phosphorylated EpoR and JAK2. Immunoblot data (fig. S10) were quantified using a CCD camera in combination with the LumiAnalyst software. Data processing, which includes merging of immunoblot data from 3 different gels, was performed with GelInspector (S7). Smoothing splines (solid lines) were applied to the data (triangles) and the threshold for integration to calculate the amount of activated EpoR and JAK2 integrated over time (Fig. 4B) was set to 10% of peak activation for stimulation with 25 U/ml Epo (dashed line).

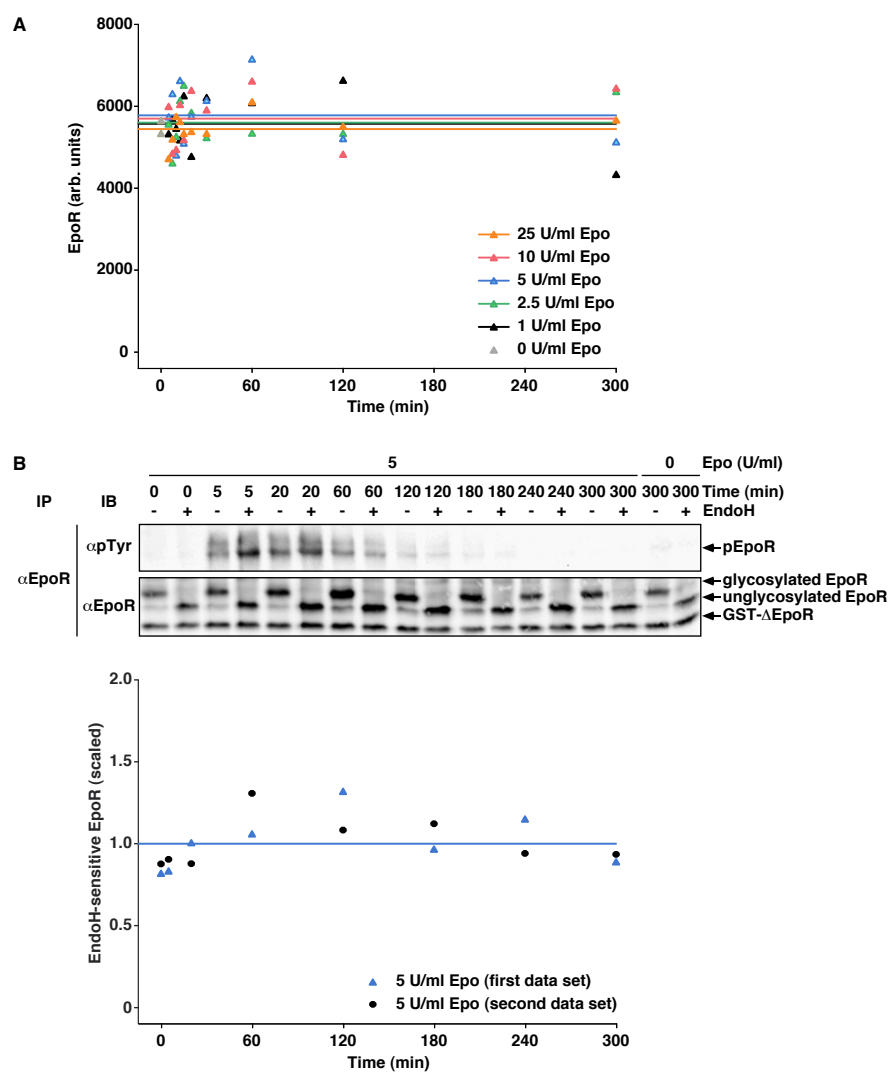


Fig. S12. Intracellular EpoR pools are in a steady-state independent of ligand stimulation. (A) Immunoblot data (fig. S10) were quantified using a CCD camera in combination with the LumiAnalyst software. Data processing, which includes merging of immunoblot data from 3 different gels, was performed with GelInspector (S7). The mean (solid lines) of data for total EpoR (triangles) is indicated. (B) BaF3-EpoR cells were stimulated with Epo or left unstimulated and subsequently lysed at the indicated time points. Immunoprecipitates (IP) were subjected to EndoH digestion or left untreated and samples were analyzed by quantitative immunoblotting (IB) with antibodies to phosphotyrosine (pTyr) and EpoR. A representative experiment is shown (upper panel). Quantification of the EndoH-sensitive EpoR (unglycosylated EpoR in EndoH-treated samples) was performed using a CCD camera in combination with the LumiAnalyst software and data (closed symbols) were processed with GelInspector (S7) for two independent experiments (lower panel). The mean (solid line) of two data sets is indicated. pEpoR, phosphorylated EpoR; GST- Δ EpoR, recombinant GST-tagged protein used as reference.

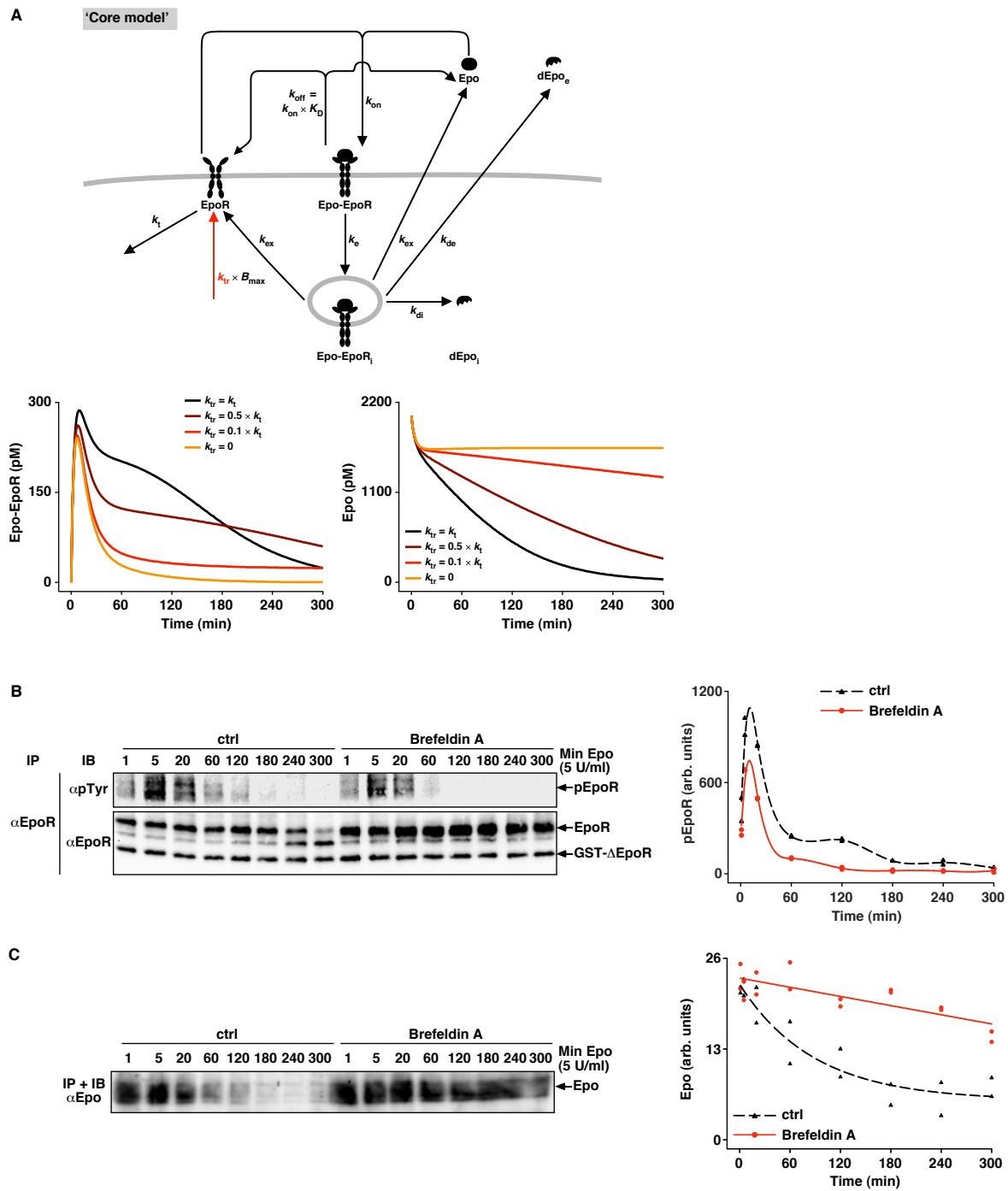


Fig. S13. Signaling through the EpoR system depends on transport of receptor from intracellular pools to the plasma membrane. (A) Model simulations for inhibited transport k_{tr} (upper panel) of receptor from intracellular pools to the plasma membrane were performed for the target quantities 'Epo-EpoR' (lower left panel) and 'Epo' (lower right panel).

panel) of the 'core model' with different inhibition efficiencies. **(B,C)** BaF3-EpoR cells were treated with 10 μ g/ml Brefeldin A or mock-treated ('ctrl') 30 min before stimulation with Epo. The culture medium was collected between 1 and 300 min and cells were subsequently lysed. Immunoprecipitated receptor from cell lysates was analyzed by immunoblotting with antibodies to phosphotyrosine (pTyr) and EpoR. Epo was immunoprecipitated (IP) from the medium and analyzed by quantitative immunoblotting (IB) with antibodies to Epo. A representative experiment is shown (left panels). Quantification of immunoblot data for two independent experiments was performed using a CCD camera in combination with the LumiAnalyst software and data were processed with GelInspector (S7) (right panels). A smoothing spline approximation and an exponential decay function were fitted to data for Brefeldin A-treated (circles, red solid line) or mock-treated samples ('ctrl', triangles, black dashed line) for **(B)** phosphorylated EpoR and **(C)** Epo, respectively. pEpoR, phosphorylated EpoR; GST- Δ EpoR, recombinant GST-tagged protein used as reference.

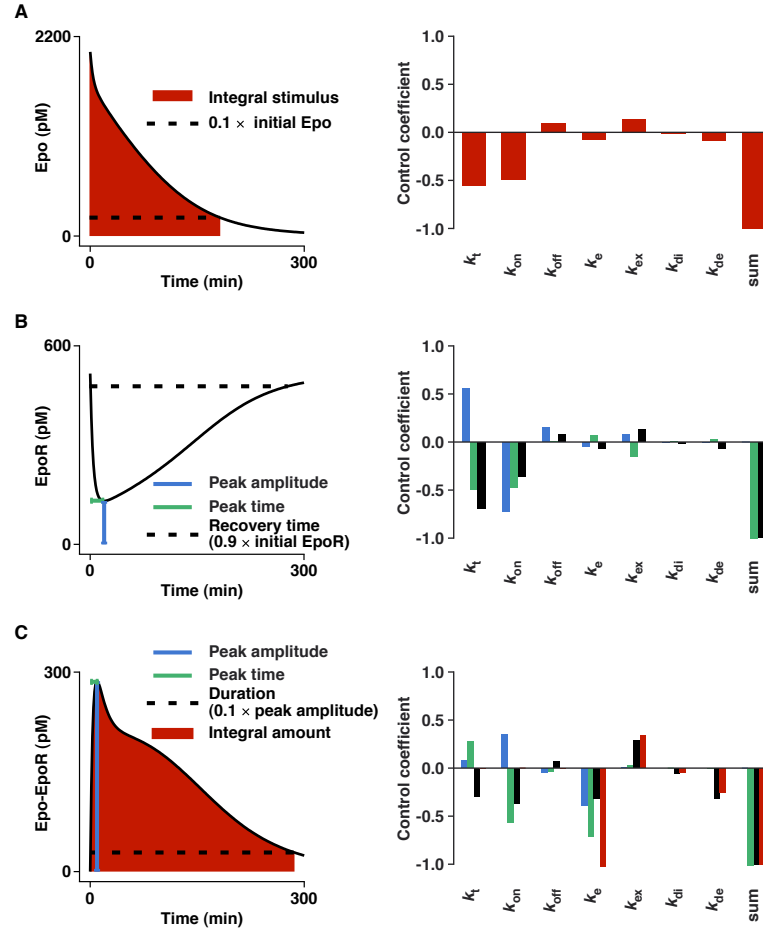


Fig. S14. Sensitivity analysis for the ‘core model’. Positive control coefficients indicate higher values for the target quantities with increasing parameter values, while negative control coefficients indicate lower values for the target quantities with increasing parameter values. Higher absolute values of control coefficients represent larger control. As shown by summation theorems, the sum of all parameters equals 0 for the target quantity ‘peak amplitude’ or -1 for all other target quantities. (A) Control coefficients were calculated for the amount of intact Epo in the culture medium integrated over time with the threshold being set to 10% of the initial value of ligand concentration. (B) Control coefficients were calculated for the peak amplitude and peak time as well as for the recovery time set to 90% of the initial EpoR concentration. (C) Control coefficients were calculated for peak amplitude, peak time, and signal duration as well as for the amount of ligand-receptor complexes integrated over time with the threshold being set to 10% of the peak value.

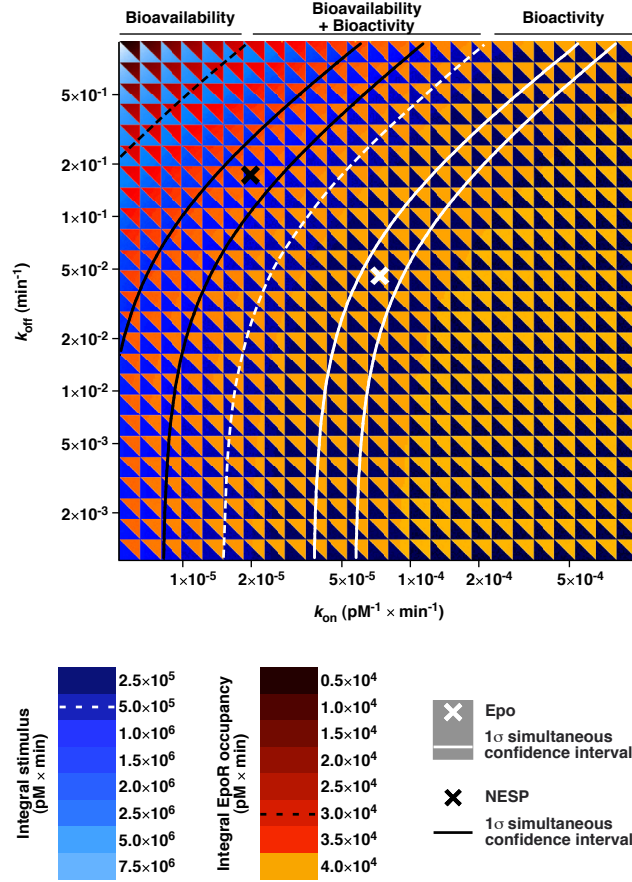


Fig. S15. Bioavailability and bioactivity of Epo derivatives. Simulations for the amount of stimulus integrated over time (integral stimulus) as well as for cell surface Epo-EpoR complexes integrated over time (integral EpoR occupancy) are displayed for different $k_{\text{on}}/k_{\text{off}}$ rate couples. Boundaries (dashed lines) may point to a desirable trade-off between bioavailability and bioactivity of erythropoiesis-stimulating agents (ESA). Values of ligand-binding kinetics for Epo (white cross) and NESP (black cross) were estimated from quantitative immunoblot data (fig. S16) and results are indicated with boundaries of 1σ simultaneous confidence intervals (solid lines).

References

- S1. R. Ketteler, S. Glaser, O. Sandra, U. M. Martens, U. Klingmüller, *Gene Ther* **9**, 477-487 (2002).
- S2. I. Swameye, T. G. Müller, J. Timmer, O. Sandra, U. Klingmüller, *Proc Natl Acad Sci U S A* **100**, 1028-1033 (2003).
- S3. A. D. Keefe, D. S. Wilson, B. Seelig, J. W. Szostak, *Protein Expr Purif* **23**, 440-446 (2001).
- S4. T. M. Kinsella, G. P. Nolan, *Hum Gene Ther* **7**, 1405-1413 (1996).
- S5. R. Palacios, M. Steinmetz, *Cell* **41**, 727-734 (1985).
- S6. S. M. Watt *et al.*, *J Cell Physiol* **115**, 37-45 (1983).
- S7. M. Schilling *et al.*, *Febs J* **272**, 6400-6411 (2005).
- S8. U. Klingmüller, U. Lorenz, L. C. Cantley, B. G. Neel, H. F. Lodish, *Cell* **80**, 729-738 (1995).
- S9. T. Maiwald, J. Timmer, *Bioinformatics* **24**, 2037-2043 (2008).
- S10. A. Raue *et al.*, *Bioinformatics* **25**, 1923-1929 (2009).
- S11. M. C. Neale, M. B. Miller, *Behav Genet* **27**, 113-120 (1997).
- S12. W. H. Press, *Numerical recipes : the art of scientific computing*. (Cambridge Univ. Press, Cambridge, ed. 3, 2007), pp. 807-817.
- S13. S. Hengl, C. Kreutz, J. Timmer, T. Maiwald, *Bioinformatics* **23**, 2612-2618 (2007).
- S14. J. J. Hornberg *et al.*, *Oncogene* **24**, 5533-5542 (2005).
- S15. J. J. Hornberg *et al.*, *Febs J* **272**, 244-258 (2005).
- S16. D. E. Quelle, F. W. Quelle, D. M. Wojchowski, *Mol. Cell. Biol.* **12**, 4553-4561 (1992).
- S17. I. Levin *et al.*, *FEBS Lett* **427**, 164-170 (1998).
- S18. G. Flint-Ashtamker, R. Eisen-Lev, J. Cohen, L. Jun-shen Huang, D. Neumann, *FEBS Lett.* **518**, 189-194 (2002).
- S19. P. Walrafen *et al.*, *Blood* **105**, 600-608 (2005).
- S20. A. W. Gross, H. F. Lodish, *J Biol Chem* **281**, 2024-2032 (2006).
- S21. R. Sulahian, O. Cleaver, L. J. Huang, *Blood* **113**, 5287-5297 (2009).
- S22. D. L. Beckman, L. L. Lin, M. E. Quinones, G. D. Longmore, *Blood* **94**, 2667-2675 (1999).
- S23. L. Meyer *et al.*, *Blood* **109**, 5215-5222 (2007).
- S24. K. S. Price *et al.*, *Am J Respir Cell Mol Biol* **28**, 420-427 (2003).
- S25. A. Yoshimura, A. D. D'Andrea, H. F. Lodish, *Proc Natl Acad Sci U S A* **87**, 4139-4143 (1990).
- S26. L. J. Huang, S. N. Constantinescu, H. F. Lodish, *Mol Cell* **8**, 1327-1338 (2001).
- S27. Z. Bajzer, A. C. Myers, S. Vuk-Pavlović, *J. Biol. Chem.* **264**, 13623-13631 (1989).
- S28. S. Belouzard, D. Delcroix, Y. Rouille, *J. Biol. Chem.* **279**, 28499-28508 (2004).
- S29. G. Carpenter, S. Cohen, *Annu Rev Biochem* **48**, 193-216 (1979).
- S30. W. Jelkmann, *Intern Med* **43**, 649-659 (2004).
- S31. H. Youssoufian, G. Longmore, D. Neumann, A. Yoshimura, H. F. Lodish, *Blood* **81**, 2223-2236 (1993).
- S32. S. N. Constantinescu *et al.*, *Proc. Natl. Acad. Sci. U.S.A.* **98**, 4379-4384 (2001).

- S33. D. Neumann, L. Wikstrom, S. S. Watowich, H. F. Lodish, *J. Biol. Chem.* **268**, 13639-13649 (1993).
- S34. S. C. Murthy, P. H. Sorensen, A. L. Mui, G. Krystal, *Blood* **73**, 1180-1187 (1989).
- S35. C. C. Reddy, S. K. Niyogi, A. Wells, H. S. Wiley, D. A. Lauffenburger, *Nat Biotechnol* **14**, 1696-1699 (1996).
- S36. H. Shankaran, H. Resat, H. S. Wiley, *PLoS Comput Biol* **3**, e101 (2007).
- S37. H. Resat, J. A. Ewald, D. A. Dixon, H. S. Wiley, *Biophys J* **85**, 730-743 (2003).
- S38. H. S. Wiley *et al.*, *J Biol Chem* **266**, 11083-11094 (1991).
- S39. P. Burke, K. Schooler, H. S. Wiley, *Mol Biol Cell* **12**, 1897-1910 (2001).
- S40. B. S. Hendriks, L. K. Opresko, H. S. Wiley, D. Lauffenburger, *Cancer Res* **63**, 1130-1137 (2003).
- S41. H. Shankaran, H. S. Wiley, H. Resat, *BMC Syst Biol* **1**, 48 (2007).
- S42. M. Martinez-Moczygemba, D. P. Huston, *J Clin Invest* **108**, 1797-1806 (2001).
- S43. A. R. Migliaccio *et al.*, *Proc Natl Acad Sci U S A* **88**, 11086-11090 (1991).
- S44. L. Supino-Rosin, A. Yoshimura, H. Altaratz, D. Neumann, *Eur J Biochem* **263**, 410-419 (1999).
- S45. D. J. Hilton, S. S. Watowich, P. J. Murray, H. F. Lodish, *Proc Natl Acad Sci U S A* **92**, 190-194 (1995).
- S46. V. Becker *et al.*, *Biochemistry* **47**, 11771-11782 (2008).
- S47. R. Ketteler *et al.*, *J Biol Chem* **277**, 26547-26552 (2002).
- S48. I. C. Macdougall, K. U. Eckardt, *Lancet* **368**, 947-953 (2006).
- S49. J. C. Egrie, J. K. Browne, *Br J Cancer* **84 Suppl 1**, 3-10 (2001).
- S50. E. L. Lehmann, Romano, J.P., *Testing statistical hypotheses*. (Springer, New York, ed. 3rd, 2005).
- S51. H. Akaike, *IEEE Trans. Automat. Control* **19**, 716-723 (1974).
- S52. G. Schwarz, *The Annals of Statistics* **6**, 461-464 (1978).